

Earth Observation and Geomatics Engineering

Online ISSN: 2588-4360

Homepage: https://eoge.ut.ac.ir/

Tomographic SAR Profiling for Buried Target Detection using Multilayer Physical **Modelling**

Somayeh Aslani-Katouli¹. Jalal Amini^{2*}. Benyamin Hosseini³



* Corresponding author

- 1. PhD Candidate in Remote Sensing, School of Surveying and Geospatial Engineering, College of Engineering, University of Tehran, Tehran, Iran. E-mail: somayeaslani.k@ut.ac.ir
- 2. Corresponding author, Full Professor, School of Surveying and Geospatial Engineering, College of Engineering, University of Tehran, Tehran, Iran. E-mail: jamini@ut.ac.ir
- 3. PhD, Remote Sensing, School of Surveying and Geospatial Engineering, College of Engineering, E-mail: s.benyamin.h@gmail.com

ABSTRACT Article Info

Article type: Research Article

Article history:

Received 2025-08-02 Received in revised form 2025-10-07 Accepted 2025-10-07 Published online 2025-10-19

Keywords:

GBSAR, tomographic profiling, Buried-target detection, Rayleigh volume scattering, *IEM*

Tomographic SAR offers a fuller description of volumetric scattering using voxels instead of pixels in SAR. The physics-based formulation incorporates multilayer propagation with Snell refraction and Fresnel transmission, moisture- and frequency-dependent dielectric behavior and attenuation per Hallikainen, and explicit surface and volume terms via the integral equation method (IEM) and Rayleigh theory. Data are focused along a sliding subaperture using a kernel that compensates refracted optical path length (OPL) while applying Fresnel and attenuation weights; an FMCW forward model with matched-filter/backprojection completes the chain. We evaluate four experiment classes: TP versus SAR, ideal versus realistic scenes, and controlled sweeps of soil moisture and soil texture. Performance is quantified by full width at half maximum (FWHM) in range and cross-range, peak sidelobe ratio (PSLR), and signal-to-background ratio (SBR). Relative to SAR, TP delivers narrower, more stable peaks and improved PSLR for buried targets. Under realistic conditions, IEM surface roughness elevates sidelobes and Rayleigh volume scattering raises the depth background, yet target localization remains stable. Increasing moisture reduces penetration and contrast, while texture primarily modulates peak width and amplitude through refractive index n and attenuation a. Overall, TP offers a practical middle ground between SAR and TomoSAR: with a single scan and appropriate windowing/sub-aperture design, it recovers an x-z depth profile that mitigates surface/volume ambiguity and improves FWHM, PSLR, and SBR compared with SAR.

Cite this article: Aslani-Katouli, S., Amini, J., & Hosseini, B. (2025). Tomographic SAR Profiling for Buried Target Detection using Multilayer Physical Modelling, Earth Observation and Geomatics Engineering, Volume 8, Issue 2, Pages 143-151. http://doi.org/10.22059/eoge.2025.403540.1191



© The Author(s).

DOI: http://doi.org/10.22059/eoge.2025.403540.1191

Publisher: University of Tehran.

1. Introduction

Imaging and understanding subsurface features is crucial for geoscience and archaeology, and exploiting the penetration capability of microwaves allows the detection of small targets close to the surface. Although GPR systems provide depth profiles, they rely on near-surface operation and slow scanning and are not efficient for large-area monitoring (Giannakis et al., 2015). In contrast, SAR systems allow for stand-off and repeatable imaging, but subsurface imaging suffers from depth ambiguity caused by the mixture of surface returns, soil volume, and buried targets (Elsherbini & Sarabandi, 2013; Fornaro et al., 2014, Fan et al., 2025; Qiao et al., 2023).

For this reason, polarimetric interferometry SAR (PolInSAR) and tomography have been proposed to provide vertical discrimination of returns. PolInSAR uses the polarization dependence of scattering mechanisms to estimate the phase center and can be generalized to height retrieval, but it does not directly provide the height distribution of backscatter within the target volume (Bamler & Hartl, 1998; Cloude & Papathanassiou, 1998; Papathanassiou & Cloude, 2001). TomoSAR offers a fuller description of volumetric scattering using voxels instead of pixels, but its main challenge is data acquisition: a set of multi-angle SAR images regularly spaced on a twodimensional aperture is required (Fortuny-Guasch & Lopez-Sanchez, 2001; Fortuny & Sieber, 1999; Lombardini et al., 2008; Reigber & Moreira, 2000). Polarization coherence tomography also promises a three-dimensional description of the target with far fewer images than multibaseline TomoSAR, yet its retrieval algorithms are modelbased and rely on assumptions about the scattering pattern (Cloude, 2006, Berenger et al., 2023).

In response to these limitations, tomographic profiling (TP) offers the opportunity to directly measure the vertical backscatter through the target volume without the constraints of multi-angle acquisitions or strong model assumptions. Using a single-pass acquisition along an aperture, TP records a wide range of incidence angles and forms a vertical profile of backscatter through the volume. Although it does not provide a full 3-D reconstruction like two-dimensional-aperture tomography, it reduces reliance on multi-angle data, and a 2-D vertical profile can mitigate the need to separate volume and surface returns (Fornaro et al., 2014; Zwieback et al., 2017).

Because the dielectric behavior of moist soil and amplitude attenuation with frequency/moisture define the physical framework (Hallikainen et al., 1985), and the IEM with semi-empirical calibrations is widely used to model backscattering and effective roughness (Baghdadi et al., 2015; Lievens et al., 2011), while pore geometry and inhomogeneity can generate significant volume scattering (Onier et al., 2010), TP was proposed as a means to extract the vertical backscatter profile from an artificial aperture (Morrison & Bennett, 2013). Building on this body of research, we develop a unified framework based on

accurate Snell refraction in layers, Hallikainen-style damping, and surface (IEM) and volume (Rayleigh) components, and implement it for a S-band FMCW sensor (named UT_GB-SAR(S)) at the Microwave Remote Sensing Laboratory of the University of Tehran. We then validate the method and assess its performance in a simulated environment using a TP processor.

2. Methods

2.1. Tomographic Profiling

Tomographic profiling (TP) is an imaging technique designed to provide vertical distribution profiles through biophysical and geophysical target volumes such as snow, ice, vegetation cover, and forest canopies.

In conventional side-looking SAR, the antenna boresight is broadside—perpendicular to the along-track direction. In TP, the antenna look direction is rotated toward the along-track plane so that, as the sensor slides along the rail, a continuum of incidence angles illuminates the scene.

2.2. Imaging algorithm

Figure 1 illustrates a full-aperture scan of length L formed by K samples with a constant spacing; any N adjacent samples constitute a sub-aperture. For a stepped-frequency continuous wave (CW) radar, to reconstruct the pixel at point P, the distances $r_1 \dots r_N$ corresponding to the chosen incidence angle i and depth z are computed, and the contribution of frequency bin m to the image at P is obtained by summing the echoes over the aperture. Using all frequency bins, the final image is formed.

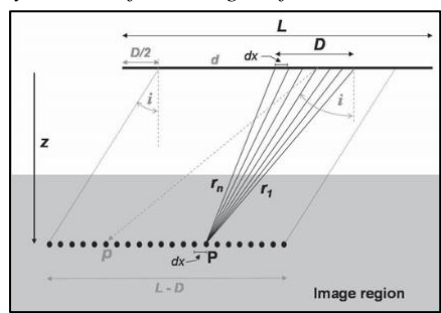


Figure 1- Demonstrate the principle of rubber band imaging technique TP (Morrison & Bennett, 2013)

A Hamming weighting window is used to reduce sidelobe ambiguity. To generate a sequence of images at fixed depth z, the focus function and measured data array are repeatedly combined; using the convolution theorem and the FFT makes this operation more efficient. As a result, the algorithm simultaneously forms the image I(x) along a line whose pixel positions are determined by the processing grid.

$$I(x) = \mathcal{F}^{-1} \left[\sum_{m=1}^{M} W(m) \mathcal{F} \{ G(x) \} \mathcal{F} \{ f(-x) \} \right]$$
 (1)

Let F and F^{-1} denote the Fourier transform and its inverse, and let G(x) be the measured data; the weighted focus function is applied in the transform domain. Because

the N samples represent a sub-aperture of K points composing the full aperture, a continuous transect image of (K - N + 1) pixels can be produced by sliding the subaperture by one sample between reconstructions.

2.3. Image resolution

Figure 2 summarizes the available resolutions for TP. Resolution in the slant-range direction (a) is controlled by bandwidth; in the direction perpendicular to slant range (b) it is controlled by the footprint of the synthetic beam. Along the synthetic beam, slant-range resolution is set by the transmitted bandwidth. In the direction perpendicular to the inclined plane, the familiar SAR relation is used.

Here, θ_{syn} is the synthetic-beamwidth, D is the artificialaperture length, i is the off-nadir (incidence) angle for a horizontal aperture, R is range, λ is wavelength, and W is the window-dependent broadening factor. Possible vertical discrimination V_a on the x-z plane (perpendicular to the scan path) follows from the combination of range and crossrange resolutions. In the exact expression, $cos(i + \theta_{syn}/2)$ replaces cos i, but since $\theta_{syn}/2$ is small it is commonly neglected. The contribution of cross-range versus range to V_a grows with tan i. The along-track (horizontal) resolution in the rail data Ha is given by the standard relation. In Figure 2 (bottom right), the scene is rotated by 90° to illustrate the true cross-track beam geometry; the real-beam resolutions res_T and H_t depend on the effective transmit/receive beamwidth Φ and on res_R. The first term in brackets arises from wavefront curvature; $\Phi/2$ is the halfpower beamwidth and cos i accounts for off-nadir projection. The vertical (V) and horizontal (H) resolutions at any image point p are then computed from the corresponding relations.

$$V_a = res_R \cos i + res_X \sin i \qquad (2)$$

$$H_a = res_R \sin i + res_X \cos i \qquad (3)$$

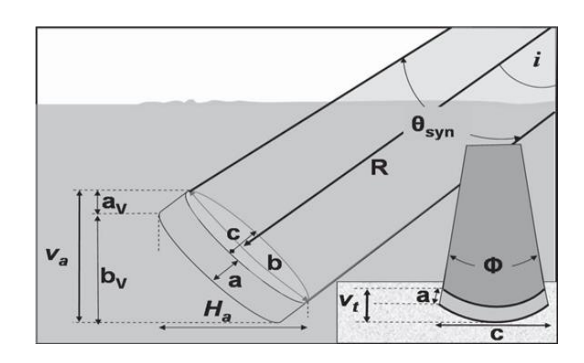


Figure 2. View Resolution available in the design (Morrison & Bennett, 2013) TP

2.4. Propagation and scattering in soil layers

This section outlines the concepts used to simulate the propagation and scattering of signals in soil layers in order to achieve a high-fidelity testbed for the processor.

Figure 3 shows the simulation flowchart.

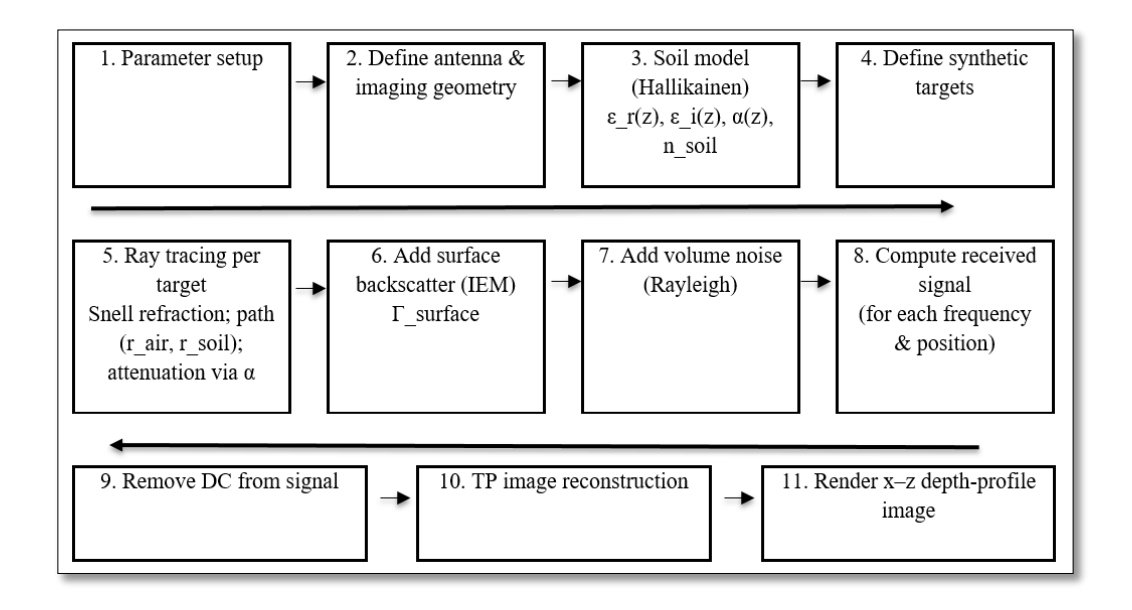


Figure 3. Simulation flowchart

2.4.1. Propagation in soil layers

Modeling soil as a lossy medium with complex permittivity $\varepsilon = \varepsilon_r - j \varepsilon_i$, the emitted signal S at depth z in soil decays exponentially with an attenuation constant α ; β is the phase constant. With the loss angle δ defined by $\tan \delta = \varepsilon_i/\varepsilon_r$, the standard relations for α and β are used. In sandy soils, $\tan \delta$ is usually small, hence $\beta \approx k \sqrt{\varepsilon}$

$$S(z) = S_0 \exp(-\gamma z) \qquad (4)$$

where: S(z) — signal amplitude at depth z; S_0 — reference amplitude at the surface; γ — attenuation constant; z — depth δ = $\arctan(\varepsilon''/\varepsilon')$ (5)

where: δ — loss angle defined as $\arctan(\varepsilon''/\varepsilon')$; ε' , ε'' — real and imaginary parts of complex permittivity $\beta = k \sqrt{\frac{\varepsilon_r}{2}} \sqrt{\sqrt{1 + \tan^2 2 \delta} + 1} \qquad (6)$

where: β — phase constant; k — wavenumber $2\pi/\lambda_0$; ε_r — relative permittivity; δ — loss angle $\alpha = k\sqrt{\frac{\varepsilon_r}{2}}\sqrt{\sqrt{1+\tan^2 2} \delta} - 1$ (7)

where: α — attenuation constant; k — wavenumber; ε_r — relative permittivity; δ — loss angle

For a layered medium, the wave path in each layer is determined by Snell's law, and the total optical path length is the sum over all layers. This can be computed analytically/numerically by solving for the refraction point on each interface (e.g., in two layers: single refraction point and two-segment propagation in upper and lower layers).

2.4.2. Snell refraction and Fresnel coefficients

The refraction point on each boundary is obtained from Fermat's principle (minimum optical length) or Snell's law. In layered environments, the refraction point is unknown a priori and must be found from the geometric solution. These conditions depend only on the refractive indices of the layers and do not determine amplitude/phase. Amplitude and phase are specified by the Fresnel coefficients, which (for a direct path to a point target) weight the transmitted/reflected waves. They first scale the energy transmitted between layers (angle- and polarization-dependent), second introduce phase shifts (in lossy/dispersive media or near critical angles), and finally help determine the dominant path (e.g., near the critical or Brewster angles). In common theradar/tomography models, refraction-point coordinates are found using Snell/OPL; then the path amplitude is computed using Hallikainen volumetric with Fresnel attenuation together two-way transmission/reflection.

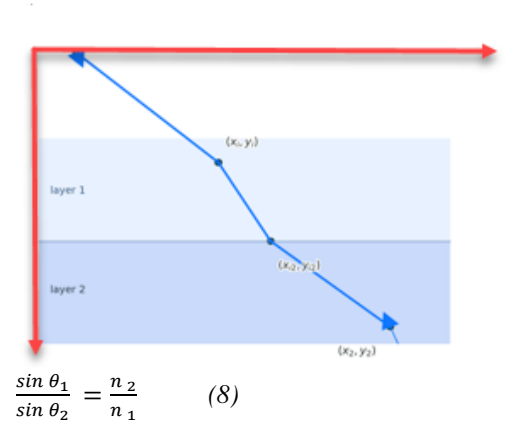


Figure 4-View of Snell's failure and failure point On the boundary of layers

$$\frac{(x_{\text{refr}} - x_{\text{ant}})}{\sqrt{(x_{\text{refr}} - x_{\text{ant}})^2 + y_{\text{ant}}^2}} \cdot \frac{(x_{\text{targ}} - x_{\text{refr}})}{\sqrt{(x_{\text{targ}} - x_{\text{refr}})^2 + y_{\text{targ}}^2}} = \frac{n_2}{n_1}$$
 (9)

$$\frac{\frac{n_1}{\mu_1}\cos\theta_i - \frac{n_2}{\mu_2}\cos\theta_t}{\frac{n_1}{\mu_1}\cos\theta_i + \frac{n_2}{\mu_2}\cos\theta_t} = S^r \qquad (10)$$

$$\frac{\frac{n_2}{\mu_2}\cos\theta_i - \frac{n_1}{\mu_1}\cos\theta_t}{\frac{n_2}{\mu_2}\cos\theta_i + \frac{n_1}{\mu_2}\cos\theta_t} = p^r \qquad (11)$$

2.4.3. Damping parameters based on the Hallikainen model

The attenuation coefficient (Np/m) is a function of ε_i and $\tan \delta$. The model provides the closed-form expressions for α and β above. To obtain ε r and ε i from soil texture and volumetric moisture mv, the Hallikainen polynomial parameterization is used.

$$\varepsilon_c = (a_0 + a_1 S + a_2 C) + (b_0 + b_1 S + b_2 C) m_v^1 + (c_0 + c_1 S + c_2 C) m_v^2$$
 (12)

2.4.4. Surface scattering with the IEM model

For moderately rough surfaces with $ks \lesssim 1$ and $k\ell \gtrsim 1$ (s rms height, ℓ correlation length, $k = 2\pi/\lambda$), the general IEM expression for $\sigma 0$ is used, where W(q) is the surfaceheight spectrum (Gaussian/exponential), and the kernels $I^{n}(n)$ -pp combine Fresnel terms and surface gradients (Long & Ulaby, 2015). $\sigma_{pp}^{0}(\theta) =$

$$\frac{k^2\cos^2\theta}{4\pi}\exp(-2k^2\sigma^2\cos^2\theta)\sum_{n=1}^{\infty}\frac{(\Psi_{pp}^n(\varepsilon,\theta))^2}{n!}WW^{(n)}(2k\sin\theta)$$
(13)

2.4.5. Volume scattering based on the Rayleigh model

For particles much smaller than the wavelength (Rayleigh regime), the single-particle scattering cross section of a sphere of radius a in a background medium of refractive-index ratio m is used (Long & Ulaby, 2015). For a layer of thickness L and number density N, σ_v^0 $\approx NL \sigma$ with one/two-way transmissivity correction.

$$\sigma_{Rayleigh} = \frac{8\pi}{3} k^4 a^6 \left| \frac{m^2 - 1}{m^2 + 2} \right|^2$$
 (14)

2.5. Sensor parameters for simulation

Table 1 shows the sensor parameters for simulation.

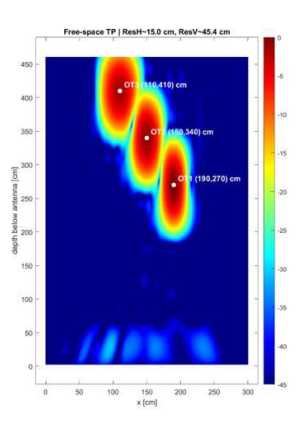
Table 1. Sensor & Scene Parameters

Parameter	Symbol	Value / Setting		
Rail length	L	≈ 3 m		
Antenna height	Z_air	≈ 1.5 m		
Band / center	S- band/fc	≈ 3.2 GHz		
		(device- specific)		
Sweep bandwidth	В	100–600 MHz (tested)		
Chirp duration	T_chirp	1–5 ms (typical)		
Spatial step	Δx	0.01-0.03 m		
Positions	K	$\approx L/\Delta x$		
Sub- aperture	D_sa	0.4–1.6 m		
Reconstruction angle	i	0°-15°		
Windowing	_	Rect / Hamming /		
		Hann / Blackman		
Polarization	pol	VV / VH / HH		

3. Experiments and Results

In this section, experiments were designed and conducted in a simulated environment, and their descriptions and results are presented.

To validate geometry and establish a performance baseline, we first consider a free- space configuration in which three point targets are placed along the rail track and imaged with a scan length of approximately $L \approx 3$ m. Design relations predict nominal resolutions of ≈ 45.4 cm in range and ≈ 15 cm in cross-range; measured point-spread widths are 59.4 cm and 21.8 cm, respectively, reflecting expected broadening from windowing and sampling. This experiment confirms the



correctness of the focusing kernel and provides a calibrated operating point for subsequent comparisons.

Figure 5. Output image of the TP processor in free space We then compare tomographic profiling (TP) with classical SAR back- projection for a single buried metal target located near x $t \approx 0$ and z $t \approx 3.40$ m. For TP, asub- aperture of D sa ≈ 1.5 m is adopted to achieve ~ 15 cm cross- range resolution. While both methods detect a peak at the true location. TP exhibits a narrower and more stable main lobe and markedly lower sidelobe levels. Aperture partitioning with appropriate frequency/space windows suppresses coherent sidelobes and stabilizes the peak position, yielding smaller effective depth FWHM and improved PSLR relative to SAR; practically, this translates into clearer detectability and more reliable localization of shallowly buried objects (Table 2; Figs. 6).

Table 2. Comparison of TP processor vs. SAR processor

Method	Δz theoretical (m)	Δz_effective (m)	FWHM (m)	PSLR (approx., dB)
SAR	_	≈ 0.45	0.50 -	-22
			0.45	-18
TP	0.15 - 0.12	≈ 0.30	0.35 -	-30
			0.28	-25

Next, we contrast an Ideal scene (specular surface, no volume scattering) with a Real scene that includes IEM surface roughness and Rayleigh volume scattering at 0° and 10° incidence. TP maintains target localization across conditions, even as the Real case exhibits higher background and slightly broader responses. The similarity of PSLR between cases indicates that sidelobes are largely controlled by the processing windows rather than the scene itself, whereas small variations with incidence angle match nominal resolution trends. These observations confirm robustness of the TP reconstruction to realistic surface/volume clutter (Table 3; Figs7).

Table 3. Quantitative results in the two scenarios

Scenario	Target	FWHM_CR	PSLR	Peak @
		(cm)	(dB)	x (cm)
Ideal 0°	A	17.7	-3.4	180.0
Ideal 0°	В	19.2	-3.1	150.0
Ideal 0°	С	20.9	-3.1	120.0
Ideal 10°	A	18.0	-3.1	180.0
Ideal 10°	В	19.1	-3.1	150.0
Ideal 10°	С	20.9	-3.1	121.0
Real 0°	A	17.7	-3.4	180.0
Real 0°	В	19.2	-3.1	150.0
Real 0°	С	20.9	-3.1	120.0
Real 10°	A	20.9	-3.0	180.0
Real 10°	В	19.0	-3.1	150.0
Real 10°	С	20.9	-3.0	121.0

We then examine moisture dependence using five levels from Dry to Wet. As moisture increases, dielectric losses rise and near- surface reflections strengthen, reducing SNR at depth and degrading target contrast. Although larger ε' can slightly sharpen the nominal depth resolution, attenuation dominates beyond moderate moisture and FWHM estimates become less reliable.

Accordingly, the best performance for deeper targets in this band is obtained at low moisture (Table 4; Figs. 8).

15

Table 4. Quantitative results vs. moisture						
Condition	ResH_th	ResV_th	FWHM_CR	FWHM_R	PSLR_CR	PSLR_R
Dry	14.88	33.204	20.525	43.217	-3.4505	-3.0999
Low	14.88	30.808	19.833	40.076	-3.0471	-3.0597
Mid	14.88	28.461	19.122	36.778	-3.2659	-1.0236
High	14.88	26.682	18.721	3860.5	-3.3829	-32.085
Wet	14.88	24.903	21.352	0	-3.4106	1.9287e-

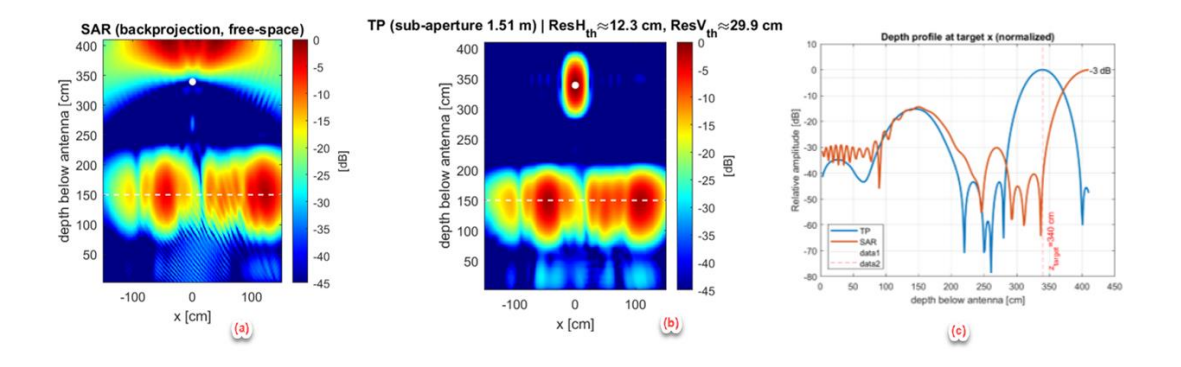


Figure 6. Free- space comparison between baseline SAR back- projection and tomographic profiling (TP). (a) SAR back- projection image; axes: x [cm] vs. depth below antenna [cm], color scale in dB. (b) TP image with a 1.51 m sub- aperture (theoretical resolutions: ResH_th \approx 12.3 cm, ResV_th \approx 29.9 cm); the white dashed line marks the depth slice used in (c). (c) Depth profile at the target x (normalized); TP exhibits a narrower -3 dB main- lobe and lower sidelobes than SA

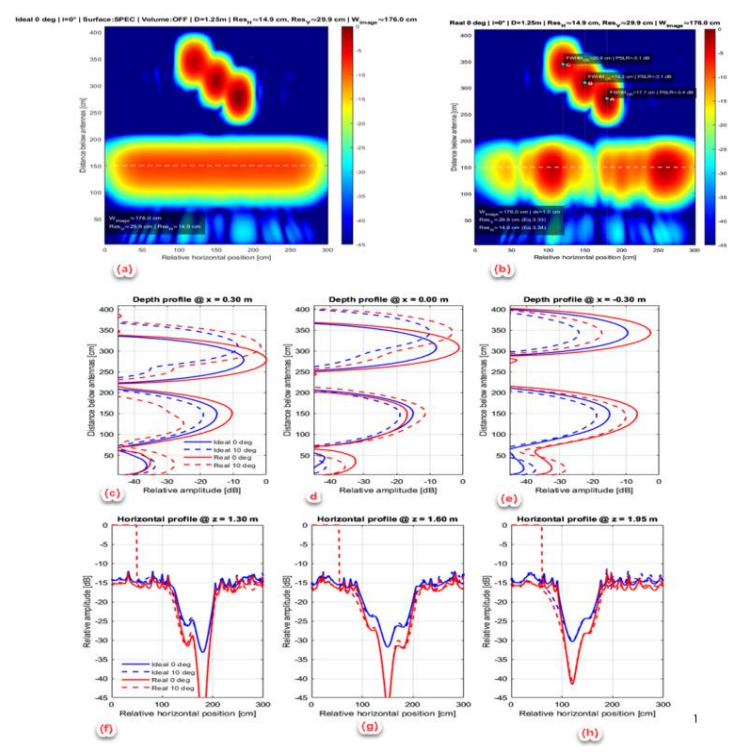
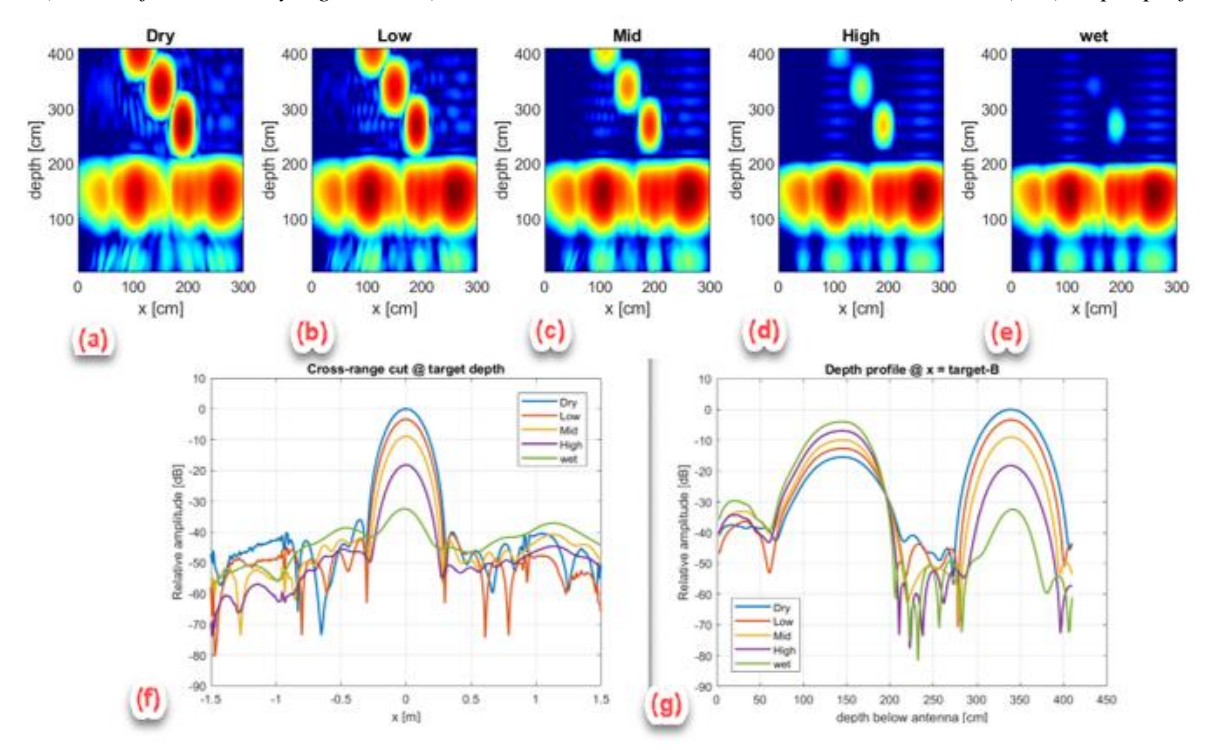


Figure 7. Ideal vs. realistic scenes at normal incidence (free - space vs. rough/volume). (a) Ideal scene TP image; (b) Realistic



scene (IEM surface with Rayleigh volume), with estimated FWHM_x annotated on inclusions; (c-e) Depth profiles at x = c

+0.30, 0.00, and -0.30 m (dashed: ideal; solid: realistic); (f-h) Cross-range (horizontal) cuts at z = 1.30, 1.60, and 1.95 m (dashed vertical lines denote the target x).

Figure 8. Moisture dependence in S-band tomographic profiling (TP).

(a—e) TP x—z reconstructions for Dry, Low, Mid, High, and Wet moisture levels; axes: x [cm] vs. depth below antenna [cm]; color scale in dB with identical normalization across panels. (f) Cross-range cut at the target depth (normalized). (g) Depth profile at x = target-B (normalized). Observation: with increasing moisture, dielectric loss and near-surface returns rise, reducing penetration and contrast; the main lobe slightly broadens and sidelobes increase (lower PSLR), while the target localization remains stable.

Finally, we analyze sensitivity to soil type using Sand, SandyLoam, Loam, Clay, and GravellySand under otherwise fixed conditions. Differences are governed primarily by permittivity and attenuation: higher refractive index n and loss a in Loam/Clay elongate range responses and reduce amplitude, whereas cross-range

behavior remains largely controlled by the chosen sub-aperture. Increased heterogeneity in GravellySand produces richer sidelobe structure and inferior PSLR. Overall, TP preserves localization and retains its FWHM/PSLR advantage relative to SAR across soil types (Table 5; Figs. 9).

Table 5. Quantitative results vs. soil type

Soil	ResH_th	ResV_th	FWHM_CR	FWHM_R	PSLR_CR	PSLR_R
Sand	14.88	29.884	19.546	38.84	-3.1335	-3.2633
SandyLoam	14.88	28.461	19.106	36.938	-3.2827	-3.1468
Loam	14.88	27.167	18.71	35.328	-3.4305	-3.4826
Clay	14.88	25.986	18.378	33.763	-3.5628	-3.2547
GravellySand	14.88	31.456	20.028	40.95	-3.637	-3.0054

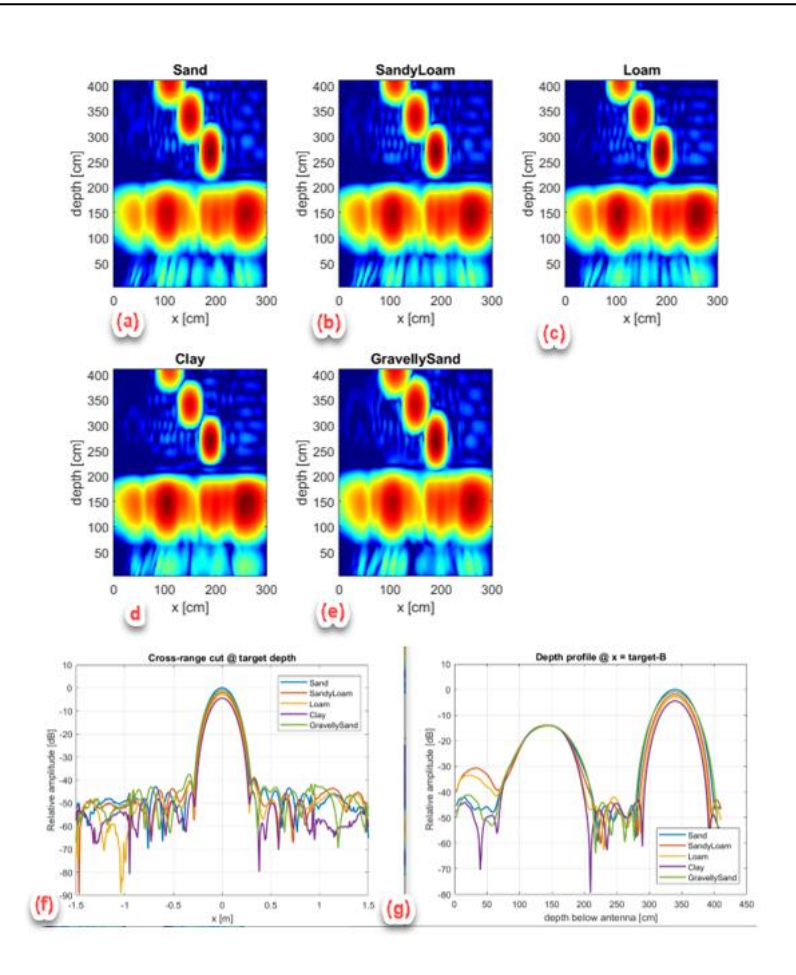


Figure 9. Soil-type sensitivity in S-band tomographic profiling (TP).

(a–e) TP x–z reconstructions for Sand, SandyLoam, Loam, Clay, and GravellySand under identical geometry and processing; axes: x [cm] vs. depth below antenna [cm]; color scale in dB with identical normalization across panels. (f) Cross-range cut at the target depth (normalized). (g) Depth profile at x = target-B (normalized). Observation: Loam/Clay (higher refractive index n and loss α) reduce peak amplitude and broaden the range response; GravellySand exhibits richer sidelobes (worse PSLR); cross-range shape is largely governed by the chosen sub-aperture, and target localization is preserved

4. Discussion

- Depth resolution and target contrast: In the comparative experiment, TP provided a smaller depth FWHM for the buried target than SAR, due to aperture partitioning and windowing that suppress sidelobes.
- Spatial stability of peaks: TP peak locations were more consistent with the reference depth—even with surface/volume clutter—than SAR, which is practically important for GB-SAR targeting.
- Scenario effects (Ideal/Real): As expected, the Real scenario had higher background due to IEM/Rayleigh contributions; PSLR was largely controlled by window selection.
- Moisture/soil: Higher moisture increased losses and reduced penetration and contrast; soil-type differences mainly reflected changes in permittivity and attenuation.

In summary, TP is an efficient middle ground between SAR and TomoSAR: with a single scan and appropriate processing, it reconstructs an x-z depth profile while reducing surface/volume ambiguity and improving FWHM, PSLR, and SBR. This advantage persists in near-realistic scenarios, with careful windowing, sub-aperture selection, and soil-parameter calibration.

5. Conclusion

This study introduced and evaluated Tomographic Profiling (TP) as a single-pass, low-cost method for retrieving vertical backscatter profiles in the S-band. Simulations showed that TP, relying on sub-aperture sliding and controlled look angle, can provide part of the advantages of TomoSAR with much simpler data acquisition and reduce the depth ambiguity typical of SAR processing. The physical framework used—multilayer propagation with Snell and Fresnel coefficients, Hallikainen moisture/frequency damping, and surface (IEM) and volume (Rayleigh) scattering—models realistic

signal behavior in soil and provides a consistent basis for analysis.

Acknowledgements

The authors gratefully acknowledge Microwave Remote Sensing Laboratory at University of Tehran for providing the radar platform and technical assistance.

References

- Baghdadi, N., Zribi, M., Paloscia, S., Verhoest, N. E. C., Lievens, H., Baup, F., & Mattia, F. (2015). Semiempirical calibration of the integral equation model for co-polarized L-band backscattering. Remote Sensing, 7(10), 13626–13640. https://doi.org/10.1088/0266-5611/14/4/001
- Bamler, R., & Hartl, P. (1998). Synthetic aperture radar interferometry. Inverse Problems, 14(4), R1. https://doi.org/10.1029/2005RS003436
- Cloude, S. R. (2006). Polarization coherence tomography. Radio Science, 41(4), 1–27. https://doi.org/10.1109/36.718859
- Cloude, S. R., & Papathanassiou, K. P. (1998). Polarimetric SAR interferometry. IEEE Transactions on Geoscience and Remote Sensing, 36(5), 1551–1565. https://doi.org/10.1109/TGRS.2013.2268388
- Elsherbini, A., & Sarabandi, K. (2013). Image distortion effects in SAR subsurface imaging and an iterative approach for refocusing and coregistration. IEEE Transactions on Geoscience and Remote Sensing, 52(5), 2994–3004. https://doi.org/10.1109/MSP.2014.2312073
- Fornaro, G., Lombardini, F., Pauciullo, A., Reale, D., & Viviani, F. (2014). Tomographic processing of interferometric SAR data. IEEE Signal Processing Magazine, 31(4), 41–50. https://doi.org/10.1109/8.954932
- Fortuny-Guasch, J., & Lopez-Sanchez, J. M. (2001). Extension of the 3-D range migration algorithm to cylindrical and spherical scanning geometries. IEEE Transactions on Antennas and Propagation, 49(10), 1434–1444. https://doi.org/10.1109/36.752219
- Fortuny, J., & Sieber, A. J. (1999). Three-dimensional SAR imaging of a fir tree: First results. IEEE Transactions on Geoscience and Remote Sensing, 37(2), 1006–1014. https://doi.org/10.1109/JSTARS.2015.2468597
- Giannakis, I., Giannopoulos, A., & Warren, C. (2015). A realistic FDTD numerical modeling framework of ground-penetrating radar for landmine detection. IEEE Journal of Selected Topics in Applied Earth Observations and Remote Sensing, 9(1), 37–51. https://doi.org/10.1109/TGRS.1985.289497
- Hallikainen, M. T., Ulaby, F. T., Dobson, M. C., El-Rayes, M. A., & Wu, L.-K. (1985). Microwave dielectric behavior of wet soil—Part I. IEEE Transactions on Geoscience and Remote Sensing, GE-23(1), 25–34. https://doi.org/10.5194/hess-15-151-2011
- Lievens, H., Verhoest, N. E. C., De Keyser, E., Vernieuwe, H., Matgen, P., Álvarez-Mozos, J., & De Baets, B. (2011). Effective roughness modelling as a tool for soil moisture retrieval from C- and L-band SAR. Hydrology

- and Earth System Sciences, 15(1), 151–162. https://doi.org/10.5194/hess-15-151-2011
- Lombardini, F., Fornaro, G., Pardini, M., Reale, D., Serafino, F., Soldovieri, F., & Costantini, M. (2008). SAR tomography for elevation and deformation reconstruction. Proc. IEEE Radar Conf., 1–7.
- Long, D., & Ulaby, F. (2015). Microwave Radar and Radiometric Remote Sensing. Artech. https://doi.org/10.1109/TGRS.2013.2250508
- Morrison, K., & Bennett, J. (2013). Tomographic profiling— A technique for multi-incidence-angle retrieval of vertical SAR backscattering profiles. IEEE Transactions on Geoscience and Remote Sensing, 52(2), 1350–1355. https://doi.org/10.1109/TGRS.2010.2053714
- Onier, C., Chanzy, A., Chambarel, A., Rouveure, R., Chanet, M., & Bolvin, H. (2010). Impact of soil structure on microwave volume scattering. IEEE Transactions on Geoscience and Remote Sensing, 49(1), 415–425. https://doi.org/10.1109/36.964971
- Papathanassiou, K. P., & Cloude, S. R. (2001). Single-baseline PolInSAR. IEEE Transactions on Geoscience and Remote Sensing, 39(11), 2352–2363. https://doi.org/10.1109/36.868873
- Reigber, A., & Moreira, A. (2000). First airborne SAR tomography demonstration using multibaseline L-band data. IEEE Transactions on Geoscience and Remote Sensing, 38(5), 2142–2152. https://doi.org/10.1109/JSTARS.2017.2671025
- Zwieback, S., Hajnsek, I., Edwards-Smith, A., & Morrison, K. (2017). Depth-resolved radar imaging of soilmoisture profiles: Observations and models of subsurface volume scattering. IEEE JSTARS, 10(7), 3281–3296.
 - https://doi.org/10.1109/JSTARS.2017.2671025
- Abassi, M., et al. (2024). Assessment of the effects of winter wheat scattering on SSRT_Oh model calibration: isotropic and Rayleigh components. Journal of the Indian Society of Remote Sensing, 52(10), 2209–2222. https://doi.org/10.1080/22797254.2024.2394780
- Berenger, Z., Denis, L., Tupin, F., Ferro- Famil, L., & Huang, Y. (2023). A deep learning approach for SAR tomographic imaging of forested areas. arXiv:2301.08605. https://doi.org/10.48550/arXiv.2301.08605
- Eide, S., Casademont, T., Aardal, Ø. L., & Hamran, S. E. (2022). Modeling FMCW Radar for Subsurface Analysis. IEEE Journal of Selected Topics in Applied Earth Observations and Remote Sensing, 15, 2998–3014. https://doi.org/10.1109/JSTARS.2022.3149019
- Fan, D., et al. (2025). A Sentinel- 1 SAR- based global 1- km soil moisture product from single- pass observations. Remote Sensing of Environment, 317, 114406. https://doi.org/10.1016/j.rse.2025.114406
- Jiang, R., et al. (2024). Estimation of soil organic carbon by combining hyperspectral and radar remote sensing to reduce coupling effects of soil surface moisture and roughness. Geoderma, 454, 116709.

 https://doi.org/10.1016/j.geoderma.2023.116709
- Qiao, H., et al. (2023). Snow profile reconstruction from tomographic UAV SAR. International Journal of Applied Earth Observation and Geoinformation, 120, 103409. https://doi.org/10.1016/j.jag.2023.103409